PNAS

Main Manuscript for

Reconfiguration of brain-wide neural activity after early life adversity.

Taylor W. Uselman[1], Russell E. Jacobs[2,3], Elaine L Bearer[1,3]

[1] University of New Mexico Health Sciences Center, Albuquerque, NM 87131
[2] Zilkha Neurogenetic Institute, Keck School of Medicine of University of Southern California, Los Angeles, CA 90033
[3] California Institute of Technology, Pasadena, CA 91125

Corresponding Author: Elaine L. Bearer
Email: elaine.bearer@gmail.com; ebearer@salud.unm.edu

Author Contributions: T.W.U. designed and performed research, contributed analytical tools, analyzed data and wrote the manuscript; R.E.J. designed and performed research, developed the imaging protocol, analyzed data and edited the manuscript; E.L.B. designed and performed research, analyzed data, wrote and edited the manuscript, and raised funding for the project.

Competing Interest Statement: The authors declare no competing interests.

Classification: Biological Sciences (Major), Neuroscience (Minor).

Keywords: manganese-enhanced magnetic resonance imaging, brain states, neuroimaging, early life adversity, acute threat

This PDF file includes:

Main Text
Figures 1 to 6

Abstract

Early life adversity (ELA) predisposes individuals to physical and mental disorders lifelong. How ELA affects brain functions, leading to these vulnerabilities, is a mystery. To understand ELA's impacts, investigations into neural activity affected by ELA must go beyond localized areas toward simultaneous recordings from multiple widely distributed regions over time. Such studies will expose relative activity between regions and discover shifts in regional activity in response to different experiences. Here, we performed longitudinal manganese-enhanced magnetic resonance imaging (MEMRI) to measure degrees of brain-wide neural activity in ELA-exposed mice across a series of experiences in adulthood. To ascertain whether ELA resulted in atypical brain activity, results were compared to those of the standard mouse (Std). MEMRI captured activity in the freely moving home cage condition, and short- and long-term after exposure to TMT, a naturalistic predator threat. Images were normalized and aligned then analyzed with statistical mapping and automated segmentation. We found that neural activity in the home cage was greater in ELA compared to Std in multiple striatal-pallidal and hypothalamic regions. Upon acute threat, neural activity in Std increased in these regions to become more similar to that in ELA, while new hyperactive responses in ELA emerged in the midbrain and hindbrain. Nine days after acute threat, heightened neural activity in ELA persisted within locus coeruleus and increased within posterior amygdala, ventral hippocampus, and dorsomedial and ventromedial hypothalamus. These results reveal functional imbalances that arise between multiple brain-systems after ELA, which are dependent upon context and cumulative experiences into adulthood.

Significance Statement

Early life adversity (ELA) is a crucial determinant of adult health. Yet the neurobiological basis for this remains elusive. Localized brain regions display atypical neural activity in rodents who experienced ELA, but how this contributes to overall brain state dynamics has been unknown. Here, we used longitudinal manganese-enhanced MRI to detect brain-wide activities altered by ELA in the adult across a series of conditions: freely moving, experiencing threat or its aftermath. Computational analyses revealed that ELA produced widespread dynamic reconfiguration of brain-wide neural activity in response to threat, shown here for the first time. Dynamic brain state remodeling after ELA provides critical insights into human mental health vulnerabilities associated with adverse childhood experiences (ACEs), and suggests plausible targets for intervention.

Main Text

Introduction

Early life adversity (ELA) poses risks for neuropsychiatric disorders, especially after a second traumatic event, such as a life-threatening experience (1-5). ELA's long-term consequences on global neural activity lasting into adulthood could serve as a biological basis for poor outcomes (6-8). We are studying the brain states of adult mice who experienced ELA to test whether neural activity in the home cage has been affected and whether their responses to threat are normal. To ascertain how a potentially normal mouse is affected by ELA into adulthood, we compared ELA-exposed mice to the standard mouse reared under generalized conditions (9, 10).

We invoked ELA in mice using a well-established paradigm: fragmented maternal care induced by limited bedding (11, 12). Most studies using preclinical paradigms focus on localized brain regions with invasive methods (13-27). Only a few have examined ELA's brain-wide consequences (28-31). Lacking are any studies that examine the brain-wide effects of threat in the adult previously exposed to ELA. Many questions remain that cannot be answered by localized techniques, such as whether brain-wide activity is changed in an adult who has experienced ELA, and whether activity in response to threat is also affected. To investigate these questions and overcome inherent limitations of other techniques, we employed longitudinal manganese-enhanced MRI (MEMRI) together with computational data-driven analysis. This provides quantitative information about global brain activity, which sometimes is described with qualitative terms for directionality or to generalize an aggregate of similar data.

Longitudinal MEMRI detects brain-wide activity before, during and after acute threat in awake freely moving mice (32, 33). Predator odor is a widely accepted naturalistic paradigm to induce innate threat responses in rodents (56-58). MEMRI does not require invasive or destructive procedures (33). Mn(II) is safe – even continuous infusion of low doses has minimal effects on behavior (33, 34). We chose to deliver Mn(II) via two single bolus injections in order to avoid surgical procedures required for continuous infusion and to allow for Mn(II) clearance between imaging sessions (32). Systemic Mn(II) distributes throughout the brain parenchyma (35), enters active neurons through voltage-gated calcium channels (36-38) and accumulates in neurons in an activity-dependent manner (33, 39, 40). MR signal intensity is proportional to the frequency of action potentials (40). Thus, MEMRI represents a quantitative readout of neural activity. Patterns of activity correspond between MEMRI and IEG expression before and after challenge (32, 38, 41). Regional accumulations of Mn(II) throughout the brain produce robust hyperintense MR signals with large

effect sizes at 100 μm^3 resolution (32, 33, 35, 41-43). These signals represent a composite picture of regional neural activity occurring between injection and imaging timepoints. Alignment of multiple MR images, collected repeatedly from large cohorts of individuals as they progress in parallel through a series of experiences, produces a dataset that enables extraction of statistically significant voxel-wise information about brain-wide activity over time, not possible with most other techniques (32, 33, 44-55). Such processing is a well-accepted practice in human imaging that yields much useful information and is routinely repurposed for rodent imaging (52, 56-59). To ensure reliability and reproducibility, computational processing is verified and validated at each step. Thus, longitudinal MEMRI can uniquely image enduring consequences of ELA on brain-wide activity in the adult and its dynamics in response to threat.

Here, we examine the consequences of ELA on adult brain-wide activity during normal home cage exploration in the adult and investigate how this activity changes in response to acute threat, short and long term, with data-driven and hypothesis-based analyses of MEMRI images captured longitudinally. Our alignments and computational processing pipeline were rigorously verified at every step. We validated Mn(II) dose by comparing signal-to-noise ratios across all individuals. We verified that Mn(II) signal replicated neural activity detected by other methods by measuring intensities in circuits known to be involved in predator odor responses and by correlation of Mn(II)-dependent enhancements with IEG (c-fos) expression. We used within- and between-group statistical parametric mapping and automated segmentation with our new *InVivo* mouse brain atlas to quantify relative activity within and between 102 segments brain-wide under each condition. We found that volumes of activities in multiple segments throughout the brain differed significantly between standard mice and those exposed to ELA undergoing the same experiential timeline.

Results

To witness neural activity in the home cage condition (HC) of adult mice who experienced ELA, and their responses to predator stress short- and long-term, we adapted our longitudinal imaging procedure (**Fig. 1A**) (32). We compared ELA mice (ELA, n = 12) to pool-weaned JAX-reared mice of the same strain (Standard, Std, n = 12) to determine whether brain-wide activity of adult mice who had experienced ELA differed from a phenotypically “normal” adult mouse and the degree of difference.

Successful Replication of Behavioral Paradigms. To test whether our protocols for these two paradigms, fragmented care (ELA) and predator stress (TMT), faithfully reproduced previously reported behaviors (60-62), we compared videos of adult mice as they explored a custom arena

(**Fig. 1B-D**). For the effect of ELA experience, we measured the time ELA mice spent in the light at baseline (BL) and compared that to Std mice. As expected, adult ELA mice spent 10% more time in the light at BL than Std, demonstrating a persisting effect of ELA experience in an unprovoked situation ($p < 0.05$ FDR, Cohen's $d = 1.58$) (**Fig. 1B**). For the effect of TMT, we measured time spent in the light and compared between BL and TMT. As expected, TMT decreased time spent in the light in both ELA and Std mice by more than 20%, demonstrating an acute effect of TMT ($p < 0.05$ FDR, Cohen's $d_{Std} = 2.29$, $d_{ELA} = 3.42$). To assess mouse recovery from MR anesthesia before being presented with TMT, we measured distance traveled in 1 min epochs and tracked movements from the beginning of a 10 min exposure to TMT (**Fig. 1C-D**). During the first minute of TMT-exposure, distance traveled was equal to or greater than that at BL. Motility then decreased by 50% or more over the 10 min TMT-exposure period ($p < 0.05$, FDR). These data support the contention that our procedures faithfully reproduced ELA and TMT paradigms, giving us confidence in assigning behavioral characteristics to unknown brain-wide activity.

Longitudinal Imaging. Our MR imaging protocol captures 8 sequential images across 12 individuals for each group (ELA and Std), yielding a total of 192 raw images with >2 million voxels each (**Fig. 1E**). To ensure no differences between groups were introduced by processing, all images were processed as a batch through our semi-automated processing pipeline (32, 33). This pipeline yielded a combined dataset of skull-stripped, intensity normalized and spatially aligned images ready for statistical evaluation. Quality assurance considerations included reviewing imaging parameters, performing SNR measurements to confirm similar Mn(II) doses, visualizing modal scaling output in voxel-by-intensity histograms to monitor equivalent intensity normalization, calculating Jaccard Similarity and Mutual Information Indices for alignment accuracy, and determining that smoothing does not significantly change regional signal intensities. All images reported here met our quality assurance standards (***SI Appendix*** **Fig. S1-2** and **Table S1**).

Brain States in Mice Exposed to ELA. To detect Mn(II)-enhancements in ELA mice across conditions from the home cage (HC) to post-threat (TMT) to nine days after threat (D9), we compared post-Mn(II) images for each condition to each mouse's respective pre-Mn(II) image using voxel-wise statistical parametric mapping (SPM) (**Fig. 2**). SPM of images at HC revealed large (16.9% of total) volumes of statistically significant signals in multiple brain regions identified by anatomy, demonstrating that the unprovoked ELA brain was already highly active ($T = 2.72$, $p < 0.01$, cluster corr.) (**Fig. 2A**). Visual inspection of SPMs revealed larger volumes of signal within regions of the olfactory bulb, striatum/pallidum, hypothalamus, hindbrain, and cerebellum, and smaller volumes within subregions of hippocampus, amygdala, and hindbrain. Immediately after TMT, volumes of statistically significant voxels increased by +1.4% overall. SPM volumes within

these regions were maintained or expanded, with sizable increases in the mid- and hindbrain (e.g., LC) (**Fig. 2B**). By D9, activity decreased in olfactory, hindbrain, and cerebellum, or increased in hippocampus, amygdala, and midbrain (e.g., PAG), leading to an overall decrease of -2.9% from HC (**Fig. 2C**). Other subregions also changed, such as a decrease of the volume of statistical signal in the lateral septum (LS) and appearance of new signal in the paraventricular nucleus of the thalamus (PVT). Direct SPM paired t-test comparisons between ELA post-Mn(II) images at each condition added to these findings from activation volumes, to also identify statistical differences in signal intensities within many regions across conditions (***SI Appendix* Fig. S3**). These findings indicate that ELA-exposed brains are already highly active before a second provocation in adulthood, and that short- and long-term brain responses to TMT have unique patterns of activity, with regions emerging or disappearing between conditions.

Magnitude of Signal Enhancements. To determine whether these statistical maps actually represent changes in intensity values across conditions, we measured intensities within 3 x 3 x 3 voxel regions of interest (ROI) in TMT-responsive regions and compared between HC and TMT (**Fig. 3A**, and ***SI Appendix* Tables S2** and **S3**) (63, 64). Our voxel-wise SPM of ELA images at HC and TMT revealed significantly enhanced signal intensities after TMT in all four expected regions ($p < 0.05$ cluster corr.) (**Fig. 3A**, *top*). At HC, SPMs show that dlOB-DII and vlAON were already enhanced and only minimally changed across conditions. Region of interest (ROI) measurements within these locations revealed that SPM signals at HC represented large signal differences over pre-Mn(II) (6.8%, dlOB-DII; 8.0%, vlAON) with standard deviations of similar magnitude, leading to large Cohen's D effect sizes ($d = 1.6$, dlOB-DII; $d = 1.5$, vlAON; $p < 0.05$ FDR). Standard deviations are shown in **Fig. 3A** and listed in ***SI Appendix* Table S3**. In aOC and aCEA, SPM signals were minimal at HC and increased from HC to TMT (**Fig. 3A**, *top*). These SPM signal changes were recapitulated in ROI comparisons, with aOC and aCEA showing small magnitudes of signal enhancement over pre-Mn(II) at HC (1.4% and 3.0%), and larger magnitudes at TMT (3.5% and 6.2%) (**Fig. 3A**, *bottom*). Thus, in this case SPMs represented signal intensity differences. Signal intensity increased in all four regions expected to respond to TMT (+2.1-3.9%, $d = 0.85$-1.20, $p < 0.05$ FDR), demonstrating robust TMT-induced enhancement.

Statistical mapping of ELA at HC (**Fig. 2** above) indicated signal enhancements within regions normally only responsive after TMT in Std (32). To determine the degree of signal intensity differences between ELA and Std at HC and test whether ELA signal truly exceeded Std in these regions, we measured and compared signal intensities within 3 x 3 x 3 voxel ROIs (**Fig. 3B**, ***SI Appendix* Tables S2** and **S4**). Magnitudes of signal enhancement at HC over pre-Mn(II) corresponded to the presence or absence of significant SPM signal for both Std and ELA (non-

enhanced: SI = 2.0-3.6%, d = 0.5-0.7; enhanced: SI = 6.1-17.9%, d = 0.96-5.17). Direct comparisons between groups revealed that ELA intensities were heightened at HC in all four measured regions (SI = 4.1-6.6%, d > 1.00, $p < 0.05$ FDR). Standard deviations are shown in **Fig. 3B** and listed in ***SI Appendix* Table S4**. Thus, ELA signal intensities within threat-responsive regions exceeded that of Std even before threat. ELA also displayed a lower variance than Std.

Together these observations support the conclusion that differences in SPM-identified activation volumes, at $p < 0.01$ and cluster size ≥ 8 voxels, reliably represent intensity differences between post-Mn(II) images. However, when SPM analysis reveals overlapping anatomy of activation volumes between groups or conditions, direct measurements of post-Mn(II) intensities may be necessary to uncover potential differences in activity levels that are not detected by activation volumes.

Mn(II)-Enhanced Signal Corresponds to c-fos Expression. We next sought to test whether differences in Mn(II)-enhancement corresponded quantitatively to differences in neural excitation, as detected by c-fos expression (33, 41, 66, 67) (**Fig. 4**). We previously reported a correspondence between c-fos and MEMRI before and after challenge (predator odor) and found similar changes in activity between the two modalities (32). Here, we compare intensity values from *in vivo* longitudinal MEMRI with positive nuclei counts from c-fos immunohistochemistry, which is an endpoint where longitudinal dynamics are not feasible. A subset of the mice that underwent the longitudinal MEMRI protocol were processed for c-fos immunohistochemistry ($n_{Std} = 5$ and $n_{ELA} = 6$). We selected pairs of regions in sections stained for c-fos where anatomy could be cross-correlated with MR slices for each mouse: hypothalamus (HYP) and thalamus (THA); superior central raphe (CS) and midbrain (MB) (**Fig. 4A-B**). First, we compared regions for each modality separately (**Fig. 4C-D**). Statistical comparison of Mn(II)-enhanced signal intensities in HYP and CS were statistically greater than in THA and MB, respectively (**Fig. 4C**, $p < 0.001$). Numbers of c-fos+ nuclei revealed similar differences between regions (**Fig. 4D**, $p < 0.001$). Robust effect sizes were observed for both modalities (c-fos: MEMRI: d = 1.88-6.37; d = 3.75-5.03). Statistical differences in MR signal intensities from this subset of mice were replicated in a second subset from each group, demonstrating test-retest reliability (d = 2.94-8.43, $p < 0.001$, FDR) (***SI Appendix* Fig. S4**). To test further whether intensities correlated linearly with c-fos counts, we calculated Pearson's pairwise correlation coefficient for MEMRI versus c-fos data across the four regions with bootstrap resampling and permutation testing. In both groups, correlations were statistically significant (Std: $r = 0.636$, $p < 0.0001$; ELA: $r = 0.582$, $p < 0.0013$) (**Fig. 4E** and ***SI Appendix* Fig. S5**).

A between-group comparison of c-fos and MEMRI at D9 for each region found that both modalities found increased activity in HYP ($d_{c\text{-}fos}$ = 0.38; d_{MEMRI} = 2.21) and CS ($d_{c\text{-}fos}$ = 1.07; d_{MEMRI} = 2.02) in ELA relative to Std. While MEMRI differences were statistically significant in HYP and CS ($p < 0.05$, FDR), c-fos differences were not, demonstrating that MEMRI could detect statistically significant differences with only 5-6 mice possibly due to larger values and smaller variance in MEMRI data. Comparison of c-fos at D9 with MEMRI from all three conditions in these regions revealed statistically significant correlations ($r > 0.582$, $p < 0.0013$). This result shows that the relative levels of activity were consistent in these regions across the longitudinal imaging procedure. Thus, our data provide evidence that differences in the degree of MEMRI signal intensities reflect differences in c-fos expression for the most part.

Deeper Dives into Brain States of Adult Mice Exposed to ELA. To assign neural activity in ELA mice to specific anatomical regions, we aligned statistical maps of enhanced voxels with our *InVivo* Atlas (***SI Appendix* Table S5**). Then we quantified activity in those anatomically defined segments at each condition with a new approach, fractional activation volumes (FAV) (32) (**Fig. 5**). The FAV is the fraction of activated to total voxels in each segment. Activated voxels were those found to be statistically enhanced in SPM comparisons of post-Mn(II) to pre-Mn(II) images at each condition. FAVs were visualized as column graphs. Comparing column graphs between conditions demonstrated changes in FAVs as mice progressed through successive conditions. For conciseness, we summarize key regional differences from this quantitative analysis using qualitative terms for direction, magnitude, and aggregate patterns. Quantitative information underlying these terms is available in ***SI Appendix* Tables S6-8**.

Overlays of statistical maps show that much of the global activity in ELA at HC (**Fig. 5A, blue**) versus pre-Mn(II) coincides with that of TMT (**Fig. 5A, red**) in the same group (**Fig. 5A, overlap purple**) ($p < 0.01$ cluster corr., d = 0.79-8.19) (***SI Appendix* Table. S6A**). Some regions expand while a few others contract from HC to TMT. By FAV analysis of ELA, we see that at HC large FAVs were prominent in various domains (OLF, STR/PAL, HYP, and CB) with some segments (MOBmi, 92%; MS, 100%; BST, 92%; and AHN, 97%) almost totally active. Immediately after TMT, FAV values were retained or increased, with the largest increases in CEA (+9%) and LC (+42%). Several STR/PAL and THA segments decreased in FAV after TMT, including LSc (-28%), LGd (-53%) and MH (-34%). No relationships between segment volume and FAV were observed. Differences in signal intensities between conditions in these segments were also statistically significant by SPM comparisons between successive post-Mn(II) images, with the greatest differences in the LC ($p < 0.05$ cluster corr.) (***SI Appendix* Fig. S6** and **Table S6B**).

249 We then compared SPM overlays and segmental FAVs between TMT (**Fig. 5B, red**) and D9 (**Fig.**
250 **5B, green; overlap, brown**) of ELA mice to learn how TMT affected brain-wide activity long term
251 (**Fig. 5B**). Segmentation analysis revealed globally that FAV decreased in three domains (OLF,
252 HB, and CB; -14% on average) with the most substantial change in CB (-19%). Most other
253 segments either retained or further increased FAV, particularly within AMY, THA, HYP and MB
254 domains (+11% on average). In many segments where FAV had increased following TMT, FAV at
255 D9 either mostly persisted (LC, 34%) or increased (CEA, +29%), suggesting a longer lasting effect
256 of the threat experience. Segments where FAV decreased acutely after TMT typically remained
257 low or further decreased (LSc, -12%). Others increased at D9 (MH, +14%). These results suggest
258 that brain activity in some segments does not return to pre-threat levels.
259
260 To test whether activities return or not to pre-threat levels, we compared HC with D9 using a similar
261 strategy in both ELA and Std mice (**Fig. 5C and 5D**, also ***SI Appendix* Table S6A**). Both overlays
262 of SPMs (**Fig. 5C and 5D, overlap, turquoise**) and columns graphs of FAV show that at D9 after
263 threat, activity in both ELA and Std was increased substantially compared to HC in many domains
264 (AMY, STR/PAL, HYP, and MB). The magnitude of FAV increase in these domains was twice as
265 large on average in Std than in ELA (+28% vs +11%). This pattern also appeared in pairwise
266 comparisons of post-Mn(II) intensities between conditions (***SI Appendix* Fig. S7** and **Table S6B**).
267 Neither the brain-wide activity of ELA nor Std returned to pre-threat levels at D9. These data
268 suggest regions in the brain remain hyperactive one week or more after acute threat.
269
270 Visual comparison of pairwise statistical maps within group at HC and D9 suggested statistical
271 differences between groups. At HC, before threat, FAVs of ELA were substantially greater than
272 those of Std across brain segments (31% vs 17% on average). These larger FAVs in ELA could
273 not be attributed to procedural differences, such as $MnCl_2$ dosing, MR parameters, imaging timing,
274 image processing, segmentation analysis (***SI Appendix* Fig. S2** and **Table S1**), differences in pre-
275 Mn(II) signal intensities between groups (***SI Appendix* Fig. S8**) or differences in anatomy between
276 groups (***SI Appendix* Fig. S9**). While Std exhibited larger FAV increases from HC to D9 than ELA
277 in most segments (+12% vs +5% on average), ELA exhibited larger increases than Std in a subset
278 of segments, including RE (+35% vs +16%) and LC (+34% vs +4%). In other segments, ELA
279 displayed the opposite directional change from HC to D9 compared to Std, including PA (+19% vs
280 -4%), LSr (-18% vs +31%), IPN (-2% vs +33%), and PCG (+19% vs -5%). Except for IPN, these
281 segments also responded acutely to TMT in ELA (**Fig. 5B**). These findings suggest that brain-wide
282 activity and its evolution from threat-naïve (HC) to threat-experienced (D9) conditions differs
283 between groups and that ELA mice resemble a post-threat-like state already at HC. Furthermore,
284 those segments that respond to TMT in ELA appear to be major contributors to differences between

285 groups at D9. These observations prompted direct between-group statistical analyses for each
286 condition.
287
288 **ELA Affected Many Segments Within Each Anatomical Domain.** To determine whether signal
289 intensities between ELA and Std differed statistically between groups, and to map the anatomical
290 distribution of those differences, we performed direct SPM comparisons. First, we performed an
291 unpaired t-test comparing baseline pre-Mn(II) images between groups, which revealed small
292 intensity differences (***SI Appendix* Fig. S7**). For subsequent comparisons, post-Mn(II) images were
293 adjusted to correct for these baseline differences. We then compared ELA and Std post-Mn(II)
294 images at each condition by an unpaired SPM t-test ($p < 0.05$, cluster corr., $d = 0.70$-5.30) (**Fig. 6**
295 and **Movie S1**). Segmentations of SPM difference maps at each condition were used to obtain the
296 number of statistically enhanced voxels (in either ELA > Std or Std > ELA) per segment, which
297 were then divided by the total number of voxels in each segment producing the fractional difference
298 volume (FDV) (**Fig. 6A-D**, and ***SI Appendix* Table S7**). At all three conditions, ELA exhibited
299 greater signal intensities than Std (i.e., heightened activity) in most segments but to a lesser extent
300 after TMT (HC, 17%; TMT 11%; D9, 12% on average), supporting observations from the within-
301 group SPMs shown in **Fig. 5**. From HC to D9, the total volume of enhanced voxels in ELA relative
302 to Std decreased by 4.4%.
303
304 Closer examination of FDVs within different anatomical domains identified heightened activity at
305 HC in ELA compared to Std within OLF (29% on average), STR/PAL (40% on average), and HYP
306 (26% on average) (**Fig. 6A**, yellow columns). At TMT, differences in these domains decreased (-
307 17% on average), although heightened HYP activity in ELA was somewhat preserved (-7%) and
308 new differences became noticeable in the CB (+16%) (**Fig. 6B**). At D9, heightened activity in the
309 HYP domain of ELA returned or even increased over HC (+13% on average) (**Fig. 6C**). While
310 heightened activity was present in most HYP segments for each condition (26% at HC vs 19% and
311 32% at TMT and D9), many other domains in ELA exhibited smaller volumes of heightened activity
312 over Std at TMT and D9, particularly segments within STR/PAL (40% at HC vs 14% at both TMT
313 and D9). In contrast, Std exhibited heightened activity compared to ELA within only a few segments
314 of CTX, THA, HYP, MB and CB domains (4.6% on average across all segments and conditions),
315 with the most differences occurring at TMT (6%) (**Fig. 6A-C**, blue columns). Thus, ELA in general
316 displayed heightened brain-wide activity over Std at HC, with FDV for ELA > Std of 10% or greater
317 in 53 of 102 total segments. Of the 53 segments, the degree of differences lessened upon
318 experiencing threat in most but not in all (TMT, 31; D9, 30). Next, we will take a deeper dive into
319 segmental activity dynamics.
320

321 Examining segment-wise FDV across conditions revealed at least five patterns of segmental
322 dynamics (**Fig. 6D**). To facilitate interpretation of activity differences across conditions, we plotted
323 FDVs indicated by arrows in **Fig. 6A-C** as line graphs (**Fig. 6D**) and FDV values listed in ***SI***
324 ***Appendix*** **Table S7**. These graphs exemplify five dynamic patterns across conditions of
325 heightened activity in ELA > Std (yellow) or Std > ELA (blue). *One* pattern was heightened activity
326 in ELA at HC, which became more similar between groups at TMT (**Fig. 6D**, blue), as exemplified
327 by MS and VMH and observed across 26 segments. Some of these segments (18) continued to be
328 similar between groups at D9 (e.g., MS) while others returned (7) to heightened activity in ELA
329 (e.g., VMH). A *second* pattern followed an opposite dynamic in response to TMT. In these
330 segments (8), volumes of heightened ELA activity expanded acutely with TMT and returned to HC
331 levels at D9 (CEA and CS, red). A *third* pattern appeared in a few segments (8), where FDVs of
332 ELA rose only at D9 (PA and DMH, green). A *fourth* pattern emerged in 5 segments (e.g., DP and
333 ARH, black). Similar to pattern one or three, ELA activities in these segments were greater than of
334 Std at HC or D9. Dissimilar to pattern one or three, ELA activities decreased in these segments
335 below those of Std at TMT. A comparison between male and female found that ELA females might
336 contribute to between-group differences at D9 in VMH, ARH and PA more than ELA males, with
337 sex-differences in PA also present in pre-Mn(II) images (***SI Appendix*** **Fig. S10**). A single segment
338 followed a *fifth* pattern (LC, purple), where activity was greater in Std at HC and then reversed after
339 TMT through D9 to become heightened in ELA. Together these data demonstrate that brain-wide
340 activity of ELA mice is reconfigured across conditions and that dynamics in response to threat, both
341 brain-wide and segment-wise, differ dramatically from Std.
342
343 **Discussion**
344
345 In this study we mapped the spatial-temporal transformations that ELA imposes on brain-wide
346 activity, as detected initially when in a home cage (HC) environment and then short and long-term
347 after challenge by an acute threat as compared to a Standard, phenotypically "normal," mouse.
348 Three different brain states (68), as defined here by widely distributed patterns of fractional
349 activation volumes among segments, emerged within each group. In all three conditions, brain
350 states of adult mice reared with the fragmented maternal care model for ELA differed from brain
351 states of adult Std mice, with greater overall neural activity after ELA (**Fig. 6E** and ***SI Appendix***
352 **Fig. S11**). Even without provocation, ELA mice at HC had heightened fractional activation volumes
353 in regions known to be activated by predator odor or altered in reward processing: olfactory and
354 hypothalamic segments (67, 69-74), as well as striatum-pallidum (32, 75, 76). Distribution of
355 heightened activity expanded immediately after threat to engage subcortical structures as well as
356 monoaminergic nuclei and deeper brainstem segments in ELA, as also occurred in Std (32). Neither

group regained HC activity patterns nine days after threat. Across all conditions, activity in hypothalamus of ELA was higher than Std. At D9, new differences emerged in the ventral hippocampus and posterior amygdala, where activity was greater in ELA. Our longitudinal brain-wide imaging strategy coupled with our computational processing and analytics empowered us to follow these brain states in the same individuals as they progress through this series of experiences in sample sizes sufficient for statistical significance. Our processing pipeline, aligning 192 whole-brain images captured with 100μm^3 resolution, allows precise localization of statistically significant activity common across multiple individuals. This unique capability is not possible with most other physiological approaches.

We found dynamic changes in segment-wise fractional activation volumes between conditions throughout the brain in both cohorts. When a segment transitions from lower to higher FAV/FDV, we predict that segment to have a more dominant functional role within its connectome. For example in ELA, the increased volume of activity In CEA (from 43% to 53%) as the mouse progresses from home cage to immediately after threat may contribute to heightened activity throughout threat circuity (77). That ELA mice sustained heightened CEA activity at all three conditions, suggests that ELA leads to persistent engagement of threat circuitry. This sustained engagement of threat circuitry after ELA may sensitize CS and LC to threat, promoting monoaminergic modulation of segmental activities toward the patterns observed at D9 (78-81). Differing levels of activity among segments of a single network across different conditions could produce different internal states (82, 83) and/or outcomes from that same network, be they actions, decisions, emotions, thoughts, memories, or creative works, such as music, poetry, or art.

Results presented here should be considered in light of several limitations. 1) Theoretically, small variations in rearing environment could contribute to differences between groups not attributable to ELA. However, multi-site studies in mice find that different breeding/rearing facilities have no effect on stress reactivity (84) and minimal explanatory value for at least 14 other physiological measures (85). JAX-reared mice are the phenotypical standard and the most commonly used mouse by researchers globally (9), making them an invaluable comparison group to generalize findings across research facilities (86). 2) Although we found minimal sex differences between male and female ELA mice, we cannot fully attribute heightened activity in HYP and vHIP/AMY segments to ELA because we only had a small sample size and because our Std group was all male. Other studies suggest a combinatorial effect of ELA and sex is likely within these threat responsive regions (73, 87, 88). 3) Small anatomical variations could have influenced our results (89-92). However, our Jacobian deformation analysis reported minimal alterations in anatomical volumes, and our SPM analysis accounted for any signal differences by preserving intensity concentrations

393 within voxels (93, 94). 4) Atlas segmentation yields volumes that vary widely, ~10^2-10^4 voxels. This
394 may miss some large segments where small- to medium-sized activations only produce small
395 fractional volumes. 5) We recognize that statistical methods are limited due to the choice of
396 thresholding and pre-preprocessing, which is particularly difficult with MRI (33, 95-97). We
397 minimized these potential issues by rigorously examining each processing step for image quality,
398 by ensuring sample size was sufficient to detect moderate to large signal enhancements from
399 Mn(II), and by selecting statistical thresholds based on effect size and false positive rate
400 corrections. Fractional volumes, pioneered here, provide quantitative detail about the volumetric
401 extent of Mn(II)-enhanced signals, and are limited by their dependence on statistical parametric
402 mapping and segmentation, and could miss variability and discrete locations of signal intensities
403 within segments. Caveats of MEMRI technology include pre-existing tissue enhancement, intensity
404 normalization procedures, and differences in dosing and imaging parameters. We have dealt with
405 each of these in detail in this study, as described above.
406
407 To what degree does Mn(II) signal faithfully represent neural activity? Staining by c-fos shown here
408 and previous reports, including IEG and non-IEG methodology, contend that Mn(II) tags active
409 neurons (32, 36-41, 98, 99). Patterns of activity in response to challenge as seen by MEMRI
410 reproduce those detected by IEG expression (32, 98). Both MEMRI and c-fos are dependent on
411 calcium entry into neurons, though minor non-voltage-gated calcium channel dependent
412 mechanisms may exist for MEMRI (99, 100). MEMRI acts as a direct, quantitative reporter of
413 electrochemical flux and neural depolarization (40). Axonal transport from an active segment to
414 another inactive segment cannot explain the timing and pattern of accumulations across the brain.
415 Therefore, we believe that Mn(II)-enhanced signals are due to activity and not secondary to
416 transport or non-voltage dependent uptake. Spatiotemporal resolution of MEMRI is less granular
417 than some other methods. At 100 μm^3 voxels, our MEMRI has higher spatial resolution than current
418 BOLD imaging but still not at the level of single neurons studied with electrophysiology. MEMRI's
419 temporal resolution is less than electrophysiology or BOLD imaging. However, MEMRI's capacity
420 for repeated longitudinal brain-wide imaging across a long time span of neural activity in awake,
421 freely moving mice makes these tradeoffs worthwhile. Thus, Mn(II)-enhanced MR signal intensities
422 and statistical activation volumes are quantitative readouts of localized neural activity across the
423 brain. MEMRI pinpoints regions and conditions worthy of study at greater resolutions by other
424 techniques.
425
426 ELA is a naturalistic translationally relevant paradigm that provides an experimental platform to test
427 neuromodulatory interventions for human adverse childhood experiences (ACEs) and the impacts
428 of subsequent life-threatening events. That brain-wide destabilization exists in adult mice after ELA

429 provides insight into neurobiological observations of mental disorders arising after ACEs in humans
430 (101, 102), where similar longitudinal studies are not feasible. Regions highlighted as being
431 particularly affected, such as locus coeruleus, raphe nuclei, and hypothalamic nuclei, suggest
432 plausible neuro-chemical or -physiological targets.
433
434 In conclusion, ELA has a brain-wide impact on balance of neural activity among widely distributed
435 sub-regions and their dynamics across a series of experiences, from freely moving exploration in
436 the home cage to immediate- and post-threat conditions. We identify specific subcomponents of
437 this brain-wide network that are differentially activated depending upon condition in adult mice who
438 experienced ELA and compare these with the standard, commonly studied, adult mouse. Future
439 studies dissecting the functional connections suggested by these MEMRI results will provide
440 valuable information on coordination of coactivated regions. A next step will be to determine the
441 functional significance of these disparate segmental activities, how they interact in a serially
442 dependent manner to reconfigure future brain states, and whether these interactions contribute to
443 vulnerabilities for mental health disorders and/or compulsive drug use. Ultimately this longitudinal
444 MEMRI technique will provide insights into neurophysiological/biochemical mechanisms
445 contributing to the reconfiguration of brain states by ELA and inspire reparative/restorative
446 interventions to protect from the harm of ELA and secondary traumatic events later in adulthood.
447
448 **Materials and Methods**
449
450 **Mice.** Animal protocols were approved by Institutional Animal Care and Use Committees at both
451 California Institute of Technology (Caltech) and University of New Mexico. Numbers were
452 determined by statistical power analyses. Both Std and ELA reared groups of C57BL/6J mice
453 (Stock No: 000664) were bred at Jackson Labs (JAX). Adults from each group went through parallel
454 acute threat timelines, were handled by the same experimentalists, and imaged at Caltech (n = 24,
455 12 in each group), in a series of experiments performed over a period of 3.8 years. For ELA, we
456 followed a fragmented care paradigm (11, 12). Longitudinal MEMRI commenced at ages 11-13 wk.
457 This age was chosen because brain development is considered largely complete by 3 months
458 (103). Equal numbers of male (n = 6) and female (n = 6) ELA pups were used from 5 weaning
459 groups. Twelve male Std mice selected from 5 different weaning cages were subjected to the
460 longitudinal experimental protocol. No litter/cage effects were detected for either group.
461
462 **Video Recordings and Acute Threat Exposure**. We followed our previously published
463 longitudinal imaging protocol (32). Briefly, prior to imaging and during TMT exposure mice were
464 tracked in a custom arena using Noldus Ethovision (XT15) (32, 104, 105). Prior to TMT exposure,

465 mice were bright, alert and responsive, and displayed normal motility. Percentage of time spent in
466 the light side of the arena and distance travelled were calculated and statistically evaluated with
467 FDR correction in R v4.2.1 (*nlme* and *emmeans* packages) (106-111). Graphs were generated in
468 R (*ggplot2*) (112).
469
470 **Longitudinal MEMRI.** After capture of a non-enhanced image, mice were injected i.p. with 0.3
471 mmol/kg of $MnCl_2$-$4H_20$ in sterile buffered saline and then imaged with contrast according to the
472 timeline previously reported (32). Between scanning sessions, video recordings, or $MnCl_2$
473 injections, mice were returned to their home cage. Mn(II) kinetics were followed by ROI analysis
474 across the timeline to test for expected intensity patterns. For optimization of MEMRI imaging
475 parameters, refer to our review (33).
476
477 **MR Image Pre-Processing.** MR images from both groups were pre-processed together in batch
478 according to standardized protocols (33, 50, 52). Briefly, raw MR image quality was visually
479 assessed and SNR quantified. Image artifacts were corrected when needed and outlier images
480 excluded from statistical analyses. Std and ELA pre- and post-Mn(II) images were then skull-
481 stripped, intensity normalized and anatomically aligned together in batch. Each processing step
482 was verified and validated (***SI Appendix* Fig. S1-2**).
483
484 **MR Image Analysis.** *Comparison of Anatomy Between Groups.* For comparison of anatomy
485 between groups, we calculated Jacobian Determinants of the Deformation fields generated by the
486 affine-nonlinear alignment step. Average Jacobian determinant values were calculated using our
487 atlas-based segmentation process (see below). Two sample t-tests between Std and ELA values
488 were performed for each segment, FDR correction.
489
490 *Measurement and Analysis of MR Intensities in ROIs.* Measurements were made from pre- and
491 post-Mn(II)-enhanced MR images that had been skull-stripped, scaled, and aligned. Coordinates
492 (x/y/z) for regions of interest (3 x 3 x 3 voxels) were selected by projecting the annotated atlas
493 labels onto the aligned grayscale template in FSLeyes and placing the crosshairs within segments
494 that appeared different in SPM comparisons to pre-Mn(II) and that corresponded to previously
495 reported TMT-responsive regions (32, 77). Intensities beyond 3 standard deviations from the
496 sample average for each ROI were considered outliers and removed; none were found. Mean
497 intensities from ROI measurements were compared by Student's paired and two-sample t-tests, or
498 by Welch's test (if heteroscedastic), in R (*t.test)*. Cohen's D effect sizes and FDR adjustments
499 (*p.adjust)* were calculated. Cohen's D for heteroscedastic data were calculated using Welch's non-
500 pooled standard deviation.

501

502 *Statistical Parametric Mapping (SPM).* For SPM, all images were smoothed to meet SPM
503 assumptions with a 0.15 mm^3 Gaussian kernel, the minimum size allowable (57, 94). We adjusted
504 for small baseline differences between groups in their pre-Mn(II) images by subtracting the average
505 voxel-wise differences of intensities from each of the ELA images. After this adjustment, an
506 unpaired t-test of pre-Mn(II) images yielded no voxels with significant differences between groups.
507 Voxel-wise T-maps of statistically significant differences between images of different conditions
508 within group (paired t-test) or between groups (unpaired t-test) were calculated using SPM12 (94).
509 Statistical maps were cluster corrected (*cluster corr.*) in SPM12 with a minimum cluster size of 8
510 voxels (94). Fiber tracts and ventricles segments were masked from statistical maps using our
511 *InVivo* Atlas. Setting statistical thresholds included consideration of minimal detectable effects and
512 smallest cluster size needed to remove false positives while minimizing loss of signal.

513

514 *Atlas Alignment, Segmentation, and Calculation of Fractional Volumes.* Our updated *InVivo* Atlas
515 grayscale image was inversely aligned to the dataset, and the warp field applied to the label image.
516 This permitted automated segmentation of the images into 117 regions, including 102 neuronal
517 clusters a.k.a. nuclei (32). Segment masks were created and applied using *fslmaths*. The number
518 of statistically enhanced voxels were identified as those from SPM paired or unpaired t-tests
519 exceeding thresholds set according to our criteria described above. The number of total voxels
520 within each segment were counted using *fslstats* (24). The fraction of enhanced voxels from SPM
521 paired (FAV) or unpaired (FDV) t-tests to total voxels within each segment were calculated in R
522 and visualized as column graphs and line plots using *ggplot2* (111-113). Segments were
523 categorized into patterns of FDV dynamics by the criteria of FDV > 0.1 for at least one condition
524 and $|\Delta FDV| > 0.1$ between conditions.

525

526 **Immunohistochemistry, c-fos Quantification and Correlation to MEMRI.** Brains from mice,
527 euthanized at the conclusion of MR imaging (5 Std and 6 ELA), were prepared for histology
528 according to our protocol (32, 114). We selected 1-3 sections also identifiable in MR slices from
529 each mouse that had regions with both very high and very low numbers of c-fos stained nuclei.
530 Nuclei were counted in a 3 x 3 grid of 100 μm^2 squares from 1-3 x 35 μm thick sections of each
531 brain, and MR intensities (SI) from each condition measured from 100 μm^3 voxels in corresponding
532 slices. Counts ranged from 0 to 27. MEMRI SI ranged from ~6,900-10,100. Counts and SI were
533 visualized in quartile boxplots with R (*ggplot2*). A square root transformation linearized c-fos+ count
534 data for determination of effect size and statistical significance. Regions counted in the same
535 section or measured in the same slice were compared statistically by linear mixed models and by
536 post-hoc paired t-tests with FDR correction. Regions were compared between groups for both

537 modalities by linear mixed models and post-hoc two-sample t-tests with FDR correction. Counts
538 and SI of each group were averaged by region and individual and then correlated, with p-value
539 determined by permutation testing.
540
541 Please see ***SI Appendix*** **Extended Methods** for additional methodological details.
542
543 **Acknowledgments**
544 We gratefully acknowledge support from the Biological Imaging Facility/Center and the Beckman
545 Institute at Caltech where imaging was performed, and funding from NIH R01MH096093 (ELB),
546 NIH NIA P20AG068077 (ELB), NIH NINDS F99NS139535 (TWU), Zilkha Neurogenetic Institute
547 (REJ) and Harvey Family Endowment (ELB). We appreciate staff, faculty and trainees at UNM,
548 USC and Caltech including Christopher S. Medina, Daniel Barto, Xiaowei Zhang and Sharon Wu
549 Lin (see ***SI Appendix***). We thank Chiara Padilla for proofreading support. We are grateful to Harry
550 B. Gray, Arnold O. Beckman Professor of Chemistry, at Caltech for insights on Mn(II)
551 metallobiology and advice on the manuscript. See ***SI Appendix*** **Additional Acknowledgements**.

552 **Figures and Tables**

553 **Figure 1.**

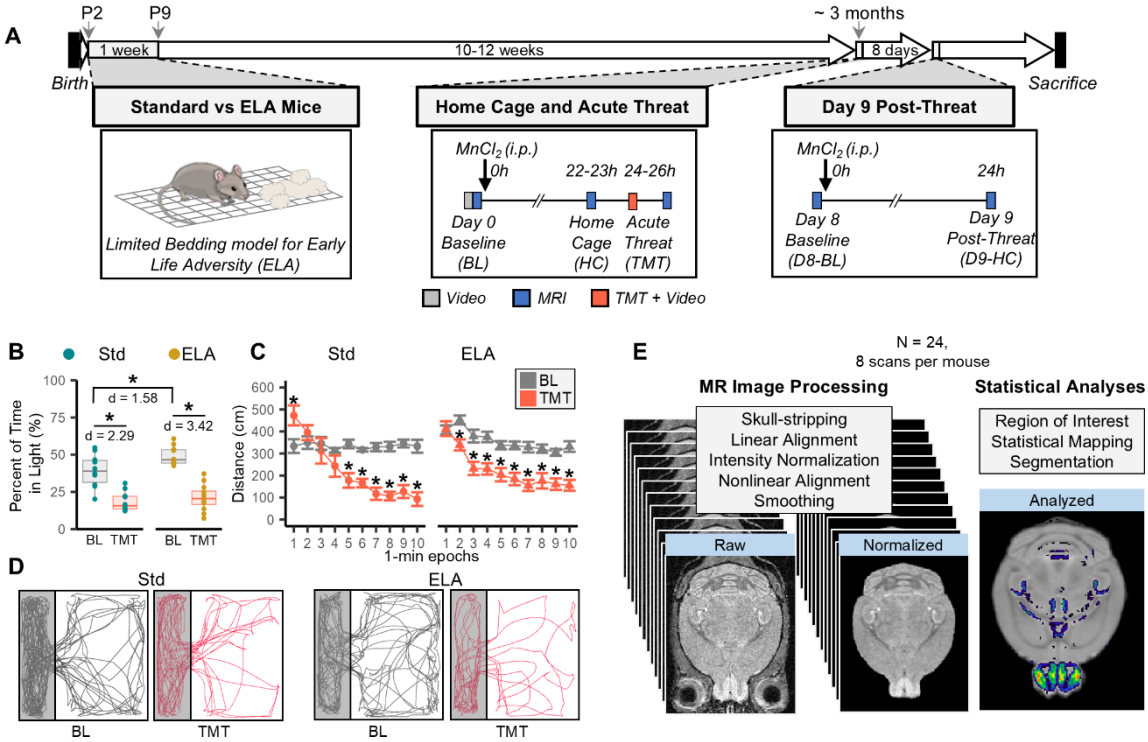

554

555 **Fig. 1.** Longitudinal imaging procedures. *(A)* Schematic of the overall timeline (open arrows, top).
556 Boxes diagram events. *Left box*: ELA paradigm; *Middle box*: Home Cage and Acute Threat, timeline
557 of MR and video capture: Baseline, BL; Home Cage, HC; Acute Threat, TMT. *Right box*: Day 8
558 Baseline, D8-BL; Day 9 Post-Threat, D9-H. *(B-D)* Video tracking results: *(B)* Percent time spent in
559 the light (quartile boxplots, individuals indicated by dot plot overlays) (cyan, Std; yellow, ELA; BL
560 and TMT as per schematic). *(C)* Distance traveled after imaging during TMT exposure. Line graphs
561 of distance travelled per 1-min epochs with error bars representing standard error of the mean.
562 Repeated measures ANOVA with fixed effects of group and condition. For (B-C), paired and
563 unpaired t-tests with FDR correction for multiple comparisons; Cohen's D effect sizes (d); * $p <$
564 0.05, n = 22 (10 Std, 12 ELA). *(D)* Representative tracking of one mouse from each group, Std and
565 ELA, at BL (gray) and TMT (red). Shaded areas represent dark side of the arena. *(E)* Overview of
566 MR data processing and analysis used in this study (also see ***SI Appendix* Fig. S1-2**) (33, 50, 52).
567

568 **Figure 2.**

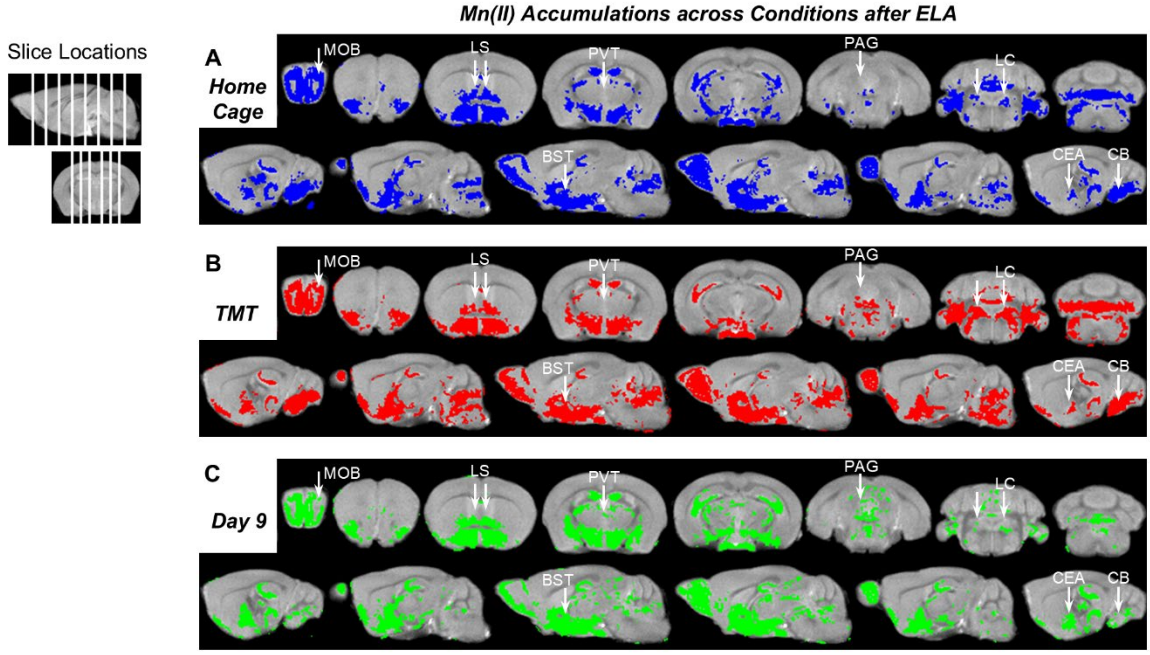

569

570 **Fig. 2.** Statistical parametric maps of MEMRI in ELA mice change as they progress from home
571 cage to acute threat to post threat. *(A-C)* Shown are statistical maps of voxel-wise paired t-tests of
572 post-Mn(II) images of ELA mice at each successive condition compared to their pre-Mn(II) images.
573 Maps are overlaid on the grayscale dataset average of all pre-Mn(II) images (coronal slices, top
574 rows; sagittal, bottom rows). Slice position is indicated on the grayscale image (top left, white lines).
575 White arrows indicate notable differences between conditions. MOB, main olfactory bulb; LS, lateral
576 septum; BST, bed nuclei of the stria terminalis; PVT, paraventricular thalamus; HIP, hippocampus;
577 LC, locus coeruleus; CEA, central amygdala; and CB, cerebellum. For t-tests, $n = 12$, $p < 0.01$, T
578 $= 2.72$, cluster corr. For comparisons between conditions of ELA mice see ***SI Appendix***, **Fig. S3**.
579

580 **Figure 3.**

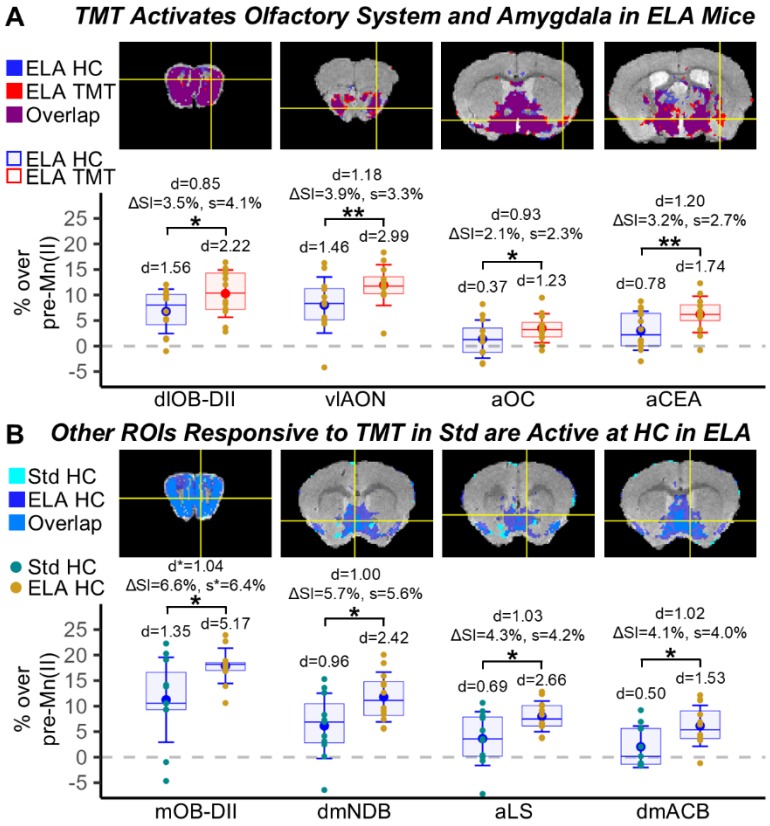

581

582 **Fig. 3.** Measurements of MEMRI signal intensities in candidate regions of interest in systems
583 known to be involved in predator odor-type threat responses. (A) Top: Representative slices from
584 two voxel-wise statistical maps (ELA HC & ELA TMT) of post-Mn(II) > pre-Mn(II) superimposed
585 onto the grayscale InVivo atlas. SPM paired t-tests: $p < 0.01$ cluster corr. ROI locations selected
586 where TMT signal did not overlap with HC (yellow crosshairs). Bottom: Quartile boxplots of signal
587 intensity as a percent over pre-Mn(II) measured in each ROI. Error bars: Mean ± standard deviation.
588 Effect sizes of the differences in signal between conditions at each ROI (Cohen's D, d), average
589 signal intensity differences (ΔSI) between the two conditions, and standard deviations of ΔSI are
590 indicated. Paired t-test, * $p < 0.05$, ** $p < 0.01$, FDR. dIOB-DII, dorsal lateral DII olfactory
591 subdomain; vlAON, ventrolateral anterior olfactory nucleus; aOC, anterior olfactory cortex; and
592 aCEA, anterior central amygdala. (B) Top: Similar comparison but between groups at one condition,
593 HC. Slices of paired t-tests of HC greater than pre-Mn(II) from either Std or ELA are superimposed
594 on the grayscale atlas. Crosshairs indicate ROI locations, selected where ELA signal did not
595 overlap with Std. Bottom: Quartile boxplots of unpaired t-tests of ROI measurements. Error bars:
596 Mean ± standard deviation. Welch's t-test and non-pooled variance-based d* and s* were used for
597 mOB-DII. * $p < 0.05$, FDR. mOB-DII, medial DII olfactory subdomain; dmNDB, dorsomedial

598 diagonal band nucleus; aLS, anterior lateral septum; dmACB, dorsomedial nucleus accumbens.
599 See ROI coordinates and summary statistics in ***SI Appendix,*** **Tables S2-4**.
600

Figure 4.

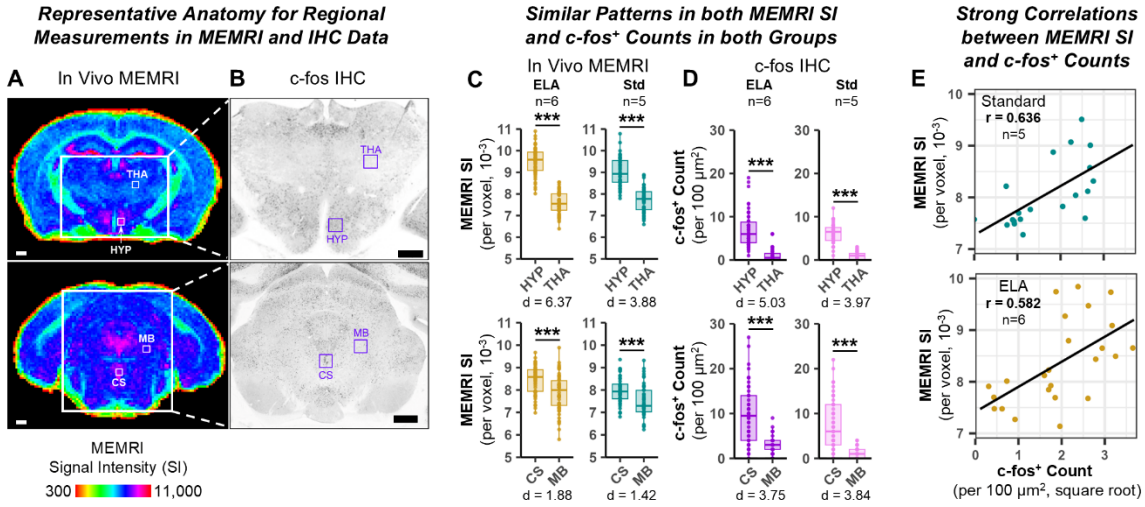

Fig. 4. MEMRI and c-fos staining correlate. (*A*) Coronal slices of the average intensities of day-9 post-Mn(II) images (color code, bottom) (n = 6). Minimum (300 a.u.) based average noise and maximum (11,000 a.u.) from intensity histograms. Small white boxes indicate regions (3 x 3 x 1 voxels) where signal intensities (SI) were measured. HYP, hypothalamus; THA, thalamus; CS, superior central raphe; MB, midbrain. Mag bar = 500 μm. (*B*) Two representative histological sections from one of the mice contributing to *(A)* stained for c-fos corresponding to anatomy of slices in *(A)* (large white boxes). Purple boxes indicate locations of 3 x 3 grid of 100 μm^2 squares where numbers of c-fos+ nuclei were counted. Mag bar = 500 μm. See ***SI Appendix* Fig. S5A-B** for corresponding images from Std. *(C)* Statistical comparisons of MEMRI SI in four locations for both groups. Shown are quartile boxplots with dot plot overlays of MEMRI SI from ELA (yellow, left) and Std (cyan, right). Paired t-tests were performed between regions within the same slice. Note large Cohen's D effect sizes (d) for paired t-tests between active and inactive regions. For evidence of test-retest reliability of MEMRI SI, see ***SI Appendix* Fig. S4**. *(D)* c-fos counts paralleled MEMRI SI with high or low numbers of c-fos+ nuclei. Shown are quartile boxplots with dot plot overlay of raw c-fos+ counts from ELA (purple, left) and Std (pink, right). A square root transformation linearized c-fos+ counts for statistics. Note similar large Cohen's D effect sizes (d) between active and inactive regions. *(E)* Strong Pearson correlations between MEMRI SI and numbers of c-fos+ nuclei (linearized) when paired by individual. Scatter plots with linear regressions (black lines) of MEMRI SI (vertical axes) by c-fos+ counts (horizontal axes). Points represent the average values for each of the 4 regions across 5 Std (*top*, *cyan*) and 6 ELA (*bottom*, *yellow*) brains. Note strong correlations in both groups (r_{Std} = 0.636, r_{ELA} = 0.582). For paired t-tests in *(C-D)*, *** $p < 0.001$, FDR corrected. For *(E)*, $p < 0.001$ by permutation testing and bootstrapping. Also see ***SI Appendix* Fig. S5C-D**.

627 **Figure 5.**

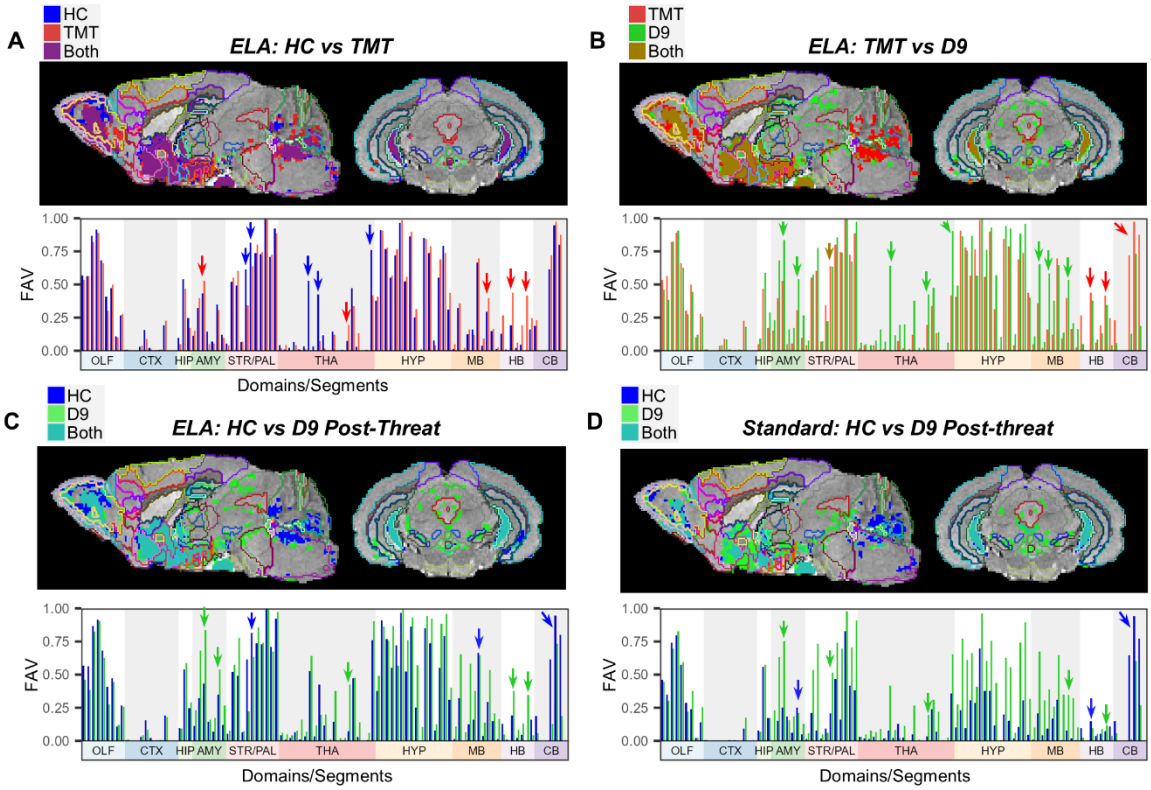

628

629 **Fig. 5.** Statistical maps show progressive modifications of activity across sequential conditions. *(A-*
630 *D)* Voxel-wise paired t-tests of post-Mn(II) compared to pre-Mn(II) images at two conditions: in ELA
631 mice, *(A)* HC (blue) and TMT (red), *(B)* TMT (red) and D9 (green), and *(C)* HC (blue) and D9
632 (green); and in Std mice, *(D)* HC (blue) and D9 (green). *Top*: Pairs of statistical maps were projected
633 onto the grayscale *InVivo* Atlas with segments outlined to show the anatomical overlaps between
634 conditions. *Bottom*: Corresponding column graphs show segment-wise fractional activation
635 volumes (FAV, vertical axes) quantified from segmentations of statistical maps. Anatomical
636 domains (color-coded on horizontal axes) are divided into 102 segments. Arrows point to examples
637 of segments with FAV alterations between conditions and color-coded to indicate direction of
638 change. For paired t-tests, $p < 0.01$, cluster *corr.* for multiple comparisons. ELA, $T_{(11)} = 2.72$, $d \geq$
639 0.79, $n = 12$; Std, $T_{(10)} = 2.76$, $d \geq 0.83$, $n = 11$. See ***SI Appendix* Table S5** for list of domains and
640 segments, and **Table S6A-B** for FAV values.

641

Figure 6.

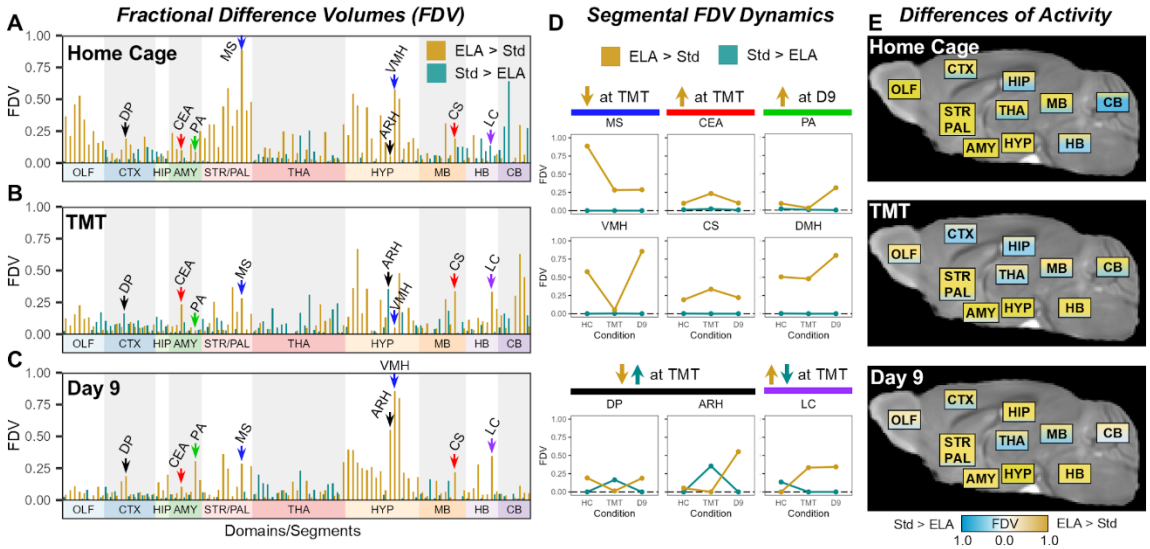

Fig. 6. ELA brain states differ from Std at every condition. *(A-C)* Fractional Difference Volumes (FDVs) from segmentation of unpaired SPM t-tests between signal intensities of ELA and Std at *(A)* HC, *(B)* TMT and *(C)* D9 conditions. All ELA images were adjusted for the voxel-wise average differences between groups' pre-Mn(II) images. FDV color-code represents where ELA signal intensities were heightened (yellow) or diminished (blue) relative to Std. Arrows in column graphs point to example segments with notable FDV dynamics as in *(D)*: blue, MS and VMH; red, CEA and CS; green, PA and DMH; black, DP and ARH; and purple, LC. *(D)* Shown are examples of various dynamics in FDV in 9 segments, which were highlighted by arrows in column graphs *(A-C)*. Line graphs show FDVs (vertical axes) of each segment across three successive conditions (horizontal axes). Graphs are grouped and color-coded according to the dynamical pattern of ELA and Std FDV values. *(A-D)* Unpaired t-tests, $p < 0.05$, cluster corr.; HC: $T_{(21)} = 1.72$, $n_{Std} = 11$, $n_{ELA} = 12$; TMT and D9: $T_{(22)} = 1.72$, n = 12 per group. *(E)* Three schematics summarizing differences in activity between ELA and Std across the 10 segmented anatomical domains at each condition: HC (*top*), TMT (*middle*) and D9 (*bottom*). Each color gradient corresponds to magnitudes and direction of segmental fractional difference volumes (FDV), and proportion of coloring indicating proportion of segments following that pattern within each domain; See **SI Appendix Movie 1** for a slice-by-slice walkthrough of between group SPMs at each condition projected on brain anatomy, **Table S8** for FDV values and **Table S6** for list of domains and segments.

663 **References**

664

665 1. Felitti VJ*, et al.* (1998) Relationship of Childhood Abuse and Household Dysfunction to
666 Many of the Leading Causes of Death in Adults. *American Journal of Preventive*
667 *Medicine* 14(4):245-258.
668 2. Merrick M*, et al.* (2019) Vital Signs: Estimated Proportion of Adult Health Problems
669 Attributable to Adverse Childhood Experiences and Implications for Prevention — 25
670 States, 2015–2017. *MMWR. Morbidity and Mortality Weekly Report* 68.
671 3. Zarse EM*, et al.* (2019) The adverse childhood experiences questionnaire: Two decades
672 of research on childhood trauma as a primary cause of adult mental illness, addiction,
673 and medical diseases. *Cogent Medicine* 6(1):1581447.
674 4. Spadoni AD*, et al.* (2022) Contribution of early-life unpredictability to neuropsychiatric
675 symptom patterns in adulthood. *Depression and Anxiety* 39(10-11):706-717.
676 5. Yehuda R*, et al.* (2010) Putative biological mechanisms for the association between early
677 life adversity and the subsequent development of PTSD. *Psychopharmacology*
678 212(3):405-417.
679 6. Chen Y & Baram TZ (2016) Toward Understanding How Early-Life Stress Reprograms
680 Cognitive and Emotional Brain Networks. *Neuropsychopharmacology* 41(1):197-206.
681 7. Kraaijenvanger EJ*, et al.* (2020) Impact of early life adversities on human brain
682 functioning: A coordinate-based meta-analysis. *Neuroscience & Biobehavioral Reviews*
683 113:62-76.
684 8. Malave L, Van Dijk MT, & Anacker C (2022) Early life adversity shapes neural circuit
685 function during sensitive postnatal developmental periods. *Translational Psychiatry*
686 12(1):306.
687 9. Garcia-Arocena D (2015) More researchers are using B6J mice than ever before. (The
688 Jackson Laboratory).
689 10. Laboratory TJ (2024) Mouse Room Conditions.
690 11. Molet J, Maras PM, Avishai-Eliner S, & Baram TZ (2014) Naturalistic rodent models of
691 chronic early-life stress. *Developmental Psychobiology* 56(8):1675-1688.
692 12. Rice CJ, Sandman CA, Lenjavi MR, & Baram TZ (2008) A Novel Mouse Model for Acute
693 and Long-Lasting Consequences of Early Life Stress. *Endocrinology* 149(10):4892-4900.
694 13. Bercum FM, Navarro Gomez MJ, & Saddoris MP (2021) Elevated fear responses to
695 threatening cues in rats with early life stress is associated with greater excitability and
696 loss of gamma oscillations in ventral-medial prefrontal cortex. *Neurobiol Learn Mem*
697 185:107541.

698 14. Bolton JL*, et al.* (2018) Anhedonia Following Early-Life Adversity Involves Aberrant
699 Interaction of Reward and Anxiety Circuits and Is Reversed by Partial Silencing of
700 Amygdala Corticotropin-Releasing Hormone Gene. *Biological Psychiatry* 83(2):137-147.
701 15. Bolton JL*, et al.* (2022) Early stress-induced impaired microglial pruning of excitatory
702 synapses on immature CRH-expressing neurons provokes aberrant adult stress
703 responses. *Cell Rep* 38(13):110600.
704 16. Brosens N, Simon C, Kessels HW, Lucassen PJ, & Krugers HJ (2023) Early life stress
705 lastingly alters the function and AMPA-receptor composition of glutamatergic synapses in
706 the hippocampus of male mice. *J Neuroendocrinol* 35(12):e13346.
707 17. de Carvalho G, Khoja S, Haile MT, & Chen LY (2023) Early life adversity impaired dorsal
708 striatal synaptic transmission and behavioral adaptability to appropriate action selection
709 in a sex-dependent manner. *Front Synaptic Neurosci* 15:1128640.
710 18. Guadagno A*, et al.* (2018) Reduced resting-state functional connectivity of the basolateral
711 amygdala to the medial prefrontal cortex in preweaning rats exposed to chronic early-life
712 stress. *Brain Struct Funct* 223(8):3711-3729.
713 19. Guadagno A, Verlezza S, Long H, Wong TP, & Walker CD (2020) It Is All in the Right
714 Amygdala: Increased Synaptic Plasticity and Perineuronal Nets in Male, But Not Female,
715 Juvenile Rat Pups after Exposure to Early-Life Stress. *The Journal of neuroscience : the*
716 *official journal of the Society for Neuroscience* 40(43):8276-8291.
717 20. Guadagno A, Wong TP, & Walker CD (2018) Morphological and functional changes in
718 the preweaning basolateral amygdala induced by early chronic stress associate with
719 anxiety and fear behavior in adult male, but not female rats. *Prog Neuropsychopharmacol*
720 *Biol Psychiatry* 81:25-37.
721 21. Gunn BG*, et al.* (2013) Dysfunctional astrocytic and synaptic regulation of hypothalamic
722 glutamatergic transmission in a mouse model of early-life adversity: relevance to
723 neurosteroids and programming of the stress response. *The Journal of neuroscience :*
724 *the official journal of the Society for Neuroscience* 33(50):19534-19554.
725 22. Johnson FK*, et al.* (2018) Amygdala hyper-connectivity in a mouse model of
726 unpredictable early life stress. *Transl Psychiatry* 8(1):49.
727 23. Kooiker CL, Chen Y, Birnie MT, & Baram TZ (2023) Genetic Tagging Uncovers a Robust,
728 Selective Activation of the Thalamic Paraventricular Nucleus by Adverse Experiences
729 Early in Life. *Biol Psychiatry Glob Open Sci* 3(4):746-755.
730 24. Levis SC*, et al.* (2022) Enduring disruption of reward and stress circuit activities by early-
731 life adversity in male rats. *Transl Psychiatry* 12(1):251.

732 25. Malter Cohen M*, et al.* (2013) Early-life stress has persistent effects on amygdala
733 function and development in mice and humans. *Proc Natl Acad Sci U S A* 110(45):18274-
734 18278.
735 26. Raineki C, Cortes MR, Belnoue L, & Sullivan RM (2012) Effects of early-life abuse differ
736 across development: infant social behavior deficits are followed by adolescent
737 depressive-like behaviors mediated by the amygdala. *The Journal of neuroscience : the*
738 *official journal of the Society for Neuroscience* 32(22):7758-7765.
739 27. Yan CG*, et al.* (2017) Aberrant development of intrinsic brain activity in a rat model of
740 caregiver maltreatment of offspring. *Transl Psychiatry* 7(1):e1005.
741 28. Holschneider DP, Guo Y, Mayer EA, & Wang Z (2016) Early life stress elicits visceral
742 hyperalgesia and functional reorganization of pain circuits in adult rats. *Neurobiol Stress*
743 3:8-22.
744 29. Islam R*, et al.* (2024) Early adversity causes sex-specific deficits in perforant pathway
745 connectivity and contextual memory in adolescent mice. *Biol Sex Differ* 15(1):39.
746 30. White JD*, et al.* (2020) Early life stress causes sex-specific changes in adult fronto-limbic
747 connectivity that differentially drive learning. *Elife* 9.
748 31. Kooiker CL*, et al.* (2024) Paraventricular Thalamus Neuronal Ensembles Encode Early-
749 life Adversity and Mediate the Consequent Sex-dependent Disruptions of Adult Reward
750 Behaviors. (Cold Spring Harbor Laboratory).
751 32. Uselman TW, Barto DR, Jacobs RE, & Bearer EL (2020) Evolution of brain-wide activity
752 in the awake behaving mouse after acute fear by longitudinal manganese-enhanced MRI.
753 *Neuroimage* 222:116975.
754 33. Uselman TW, Medina CS, Gray HB, Jacobs RE, & Bearer EL (2022) Longitudinal
755 manganese-enhanced magnetic resonance imaging of neural projections and
756 activity.e4675.
757 34. Vousden DA*, et al.* (2018) Continuous manganese delivery via osmotic pumps for
758 manganese-enhanced mouse MRI does not impair spatial learning but leads to skin
759 ulceration. *NeuroImage* 173:411-420.
760 35. Aoki I, Wu YJ, Silva AC, Lynch RM, & Koretsky AP (2004) In vivo detection of
761 neuroarchitecture in the rodent brain using manganese-enhanced MRI. *Neuroimage*
762 22(3):1046-1059.
763 36. Bedenk BT*, et al.* (2018) Mn(2+) dynamics in manganese-enhanced MRI (MEMRI):
764 Cav1.2 channel-mediated uptake and preferential accumulation in projection terminals.
765 *Neuroimage* 169:374-382.
766 37. Narita K, Kawasaki F, & Kita H (1990) Mn and Mg influxes through Ca channels of motor
767 nerve terminals are prevented by verapamil in frogs. *Brain research* 510(2):289-295.

768 38. Hattori S*, et al.* (2013) In vivo evaluation of cellular activity in alphaCaMKII heterozygous
769 knockout mice using manganese-enhanced magnetic resonance imaging (MEMRI). *Front*
770 *Integr Neurosci* 7:76.
771 39. Lin YJ & Koretsky AP (1997) Manganese ion enhances T1-weighted MRI during brain
772 activation: an approach to direct imaging of brain function. *Magnetic resonance in*
773 *medicine* 38(3):378-388.
774 40. Svehla P, Bedecarrats A, Jahn C, Nargeot R, & Ciobanu L (2018) Intracellular
775 manganese enhanced MRI signals reflect the frequency of action potentials in Aplysia
776 neurons. *J Neurosci Methods* 295:121-128.
777 41. Malkova NV, Gallagher JJ, Yu CZ, Jacobs RE, & Patterson PH (2014) Manganese-
778 enhanced magnetic resonance imaging reveals increased DOI-induced brain activity in a
779 mouse model of schizophrenia. *Proc Natl Acad Sci U S A* 111(24):E2492-2500.
780 42. Yu X, Sanes DH, Aristizabal O, Wadghiri YZ, & Turnbull DH (2007) Large-scale
781 reorganization of the tonotopic map in mouse auditory midbrain revealed by MRI.
782 *Proceedings of the National Academy of Sciences* 104(29):12193-12198.
783 43. Yu X, Wadghiri YZ, Sanes DH, & Turnbull DH (2005) In vivo auditory brain mapping in
784 mice with Mn-enhanced MRI. *Nature Neuroscience* 8(7):961-968.
785 44. Bearer EL*, et al.* (2007) Role of neuronal activity and kinesin on tract tracing by
786 manganese-enhanced MRI (MEMRI). *Neuroimage* 37 Suppl 1:S37-46.
787 45. Bearer EL, Zhang X, & Jacobs RE (2007) Live imaging of neuronal connections by
788 magnetic resonance: Robust transport in the hippocampal–septal memory circuit in a
789 mouse model of Down syndrome. *NeuroImage* 37(1):230-242.
790 46. Bearer EL, Zhang X, Janvelyan D, Boulat B, & Jacobs RE (2009) Reward circuitry is
791 perturbed in the absence of the serotonin transporter. *Neuroimage* 46(4):1091-1104.
792 47. Zhang X*, et al.* (2010) Altered neurocircuitry in the dopamine transporter knockout mouse
793 brain. *PLoS One* 5(7):e11506.
794 48. Gallagher JJ, Zhang X, Ziomek GJ, Jacobs RE, & Bearer EL (2012) Deficits in axonal
795 transport in hippocampal-based circuitry and the visual pathway in APP knock-out
796 animals witnessed by manganese enhanced MRI. *Neuroimage* 60(3):1856-1866.
797 49. Gallagher JJ*, et al.* (2013) Altered reward circuitry in the norepinephrine transporter
798 knockout mouse. *PLoS One* 8(3):e57597.
799 50. Delora A*, et al.* (2016) A simple rapid process for semi-automated brain extraction from
800 magnetic resonance images of the whole mouse head. *J Neurosci Methods* 257:185-193.
801 51. Medina CS*, et al.* (2017) Hippocampal to basal forebrain transport of Mn(2+) is impaired
802 by deletion of KLC1, a subunit of the conventional kinesin microtubule-based motor.
803 *Neuroimage* 145(Pt A):44-57.

804 52. Medina CS, Manifold-Wheeler B, Gonzales A, & Bearer EL (2017) Automated
805 Computational Processing of 3-D MR Images of Mouse Brain for Phenotyping of Living
806 Animals. *Curr Protoc Mol Biol* 119:29A 25 21-29A 25 38.
807 53. Bearer EL*, et al.* (2018) Alterations of functional circuitry in aging brain and the impact of
808 mutated APP expression. *Neurobiol Aging* 70:276-290.
809 54. Bearer EL, Barto D, & Jacobs RE (2019) Imaging the evolution acute fear: Longitudinal
810 whole brain imaging in living mice of neural activity with MEMRI. *Proceedings of the*
811 *International Society for Magnetic Resonance in Medicine... Scientific Meeting and*
812 *Exhibition. International Society for Magnetic Resonance in Medicine. Scientific Meeting*
813 *and Exhibition*, (NIH Public Access).
814 55. Medina CS*, et al.* (2019) Decoupling the Effects of the Amyloid Precursor Protein From
815 Amyloid-beta Plaques on Axonal Transport Dynamics in the Living Brain. *Front Cell*
816 *Neurosci* 13:501.
817 56. Phinyomark A, Ibanez-Marcelo E, & Petri G (2017) Resting-State fMRI Functional
818 Connectivity: Big Data Preprocessing Pipelines and Topological Data Analysis. *IEEE*
819 *Transactions on Big Data* 3(4):415-428.
820 57. Flandin G & Friston K (2008) Statistical parametric mapping (SPM). *Scholarpedia*
821 3(4):6232.
822 58. Penny WD, Friston KJ, Ashburner JT, Kiebel SJ, & Nichols TE (2011) *Statistical*
823 *Parametric Mapping: The Analysis of Functional Brain Images* (Elsevier Science).
824 59. Pallast N*, et al.* (2019) Processing Pipeline for Atlas-Based Imaging Data Analysis of
825 Structural and Functional Mouse Brain MRI (AIDAmri). *Frontiers in Neuroinformatics* 13.
826 60. Fendt M, Endres T, Lowry CA, Apfelbach R, & McGregor IS (2005) TMT-induced
827 autonomic and behavioral changes and the neural basis of its processing. *Neuroscience*
828 *and biobehavioral reviews* 29(8):1145-1156.
829 61. Rosen J, Asok A, & Chakraborty T (2015) The smell of fear: innate threat of 2,5-dihydro-
830 2,4,5-trimethylthiazoline, a single molecule component of a predator odor. 9.
831 62. Gallo M*, et al.* (2019) Limited Bedding and Nesting Induces Maternal Behavior
832 Resembling Both Hypervigilance and Abuse. 13.
833 63. Matsukawa M, Yoshikawa M, Katsuyama N, Aizawa S, & Sato T (2022) The Anterior
834 Piriform Cortex and Predator Odor Responses: Modulation by Inhibitory Circuits. *Front*
835 *Behav Neurosci* 16:896525.
836 64. Matsumoto H*, et al.* (2010) Spatial Arrangement of Glomerular Molecular-Feature
837 Clusters in the Odorant-Receptor Class Domains of the Mouse Olfactory Bulb.
838 103(6):3490-3500.
839 65. Cohen J (2013) Statistical Power Analysis for the Behavioral Sciences.

840 66. Kimbrough A*, et al.* (2020) Brain-wide functional architecture remodeling by alcohol
841 dependence and abstinence. 117(4):2149-2159.
842 67. Motta SC*, et al.* (2009) Dissecting the brain's fear system reveals the hypothalamus is
843 critical for responding in subordinate conspecific intruders. *Proceedings of the National*
844 *Academy of Sciences* 106(12):4870-4875.
845 68. Greene AS, Horien C, Barson D, Scheinost D, & Constable RT (2023) Why is everyone
846 talking about brain state? *Trends Neurosci* 46(7):508-524.
847 69. Ben-Shaul Y, Katz LC, Mooney R, & Dulac C (2010) In vivo vomeronasal stimulation
848 reveals sensory encoding of conspecific and allospecific cues by the mouse accessory
849 olfactory bulb. 107(11):5172-5177.
850 70. Canteras NS (2002) The medial hypothalamic defensive system: Hodological
851 organization and functional implications. *Pharmacology Biochemistry and Behavior*
852 71(3):481-491.
853 71. Canteras NS, Chiavegatto S, Ribeiro do Valle LE, & Swanson LW (1997) Severe
854 Reduction of Rat Defensive Behavior to a Predator by Discrete Hypothalamic Chemical
855 Lesions. *Brain Research Bulletin* 44(3):297-305.
856 72. Janitzky K, D′Hanis W, Kröber A, & Schwegler H (2015) TMT predator odor activated
857 neural circuit in C57BL/6J mice indicates TMT-stress as a suitable model for
858 uncontrollable intense stress. *Brain research* 1599:1-8.
859 73. Kunwar PS*, et al.* (2015) Ventromedial hypothalamic neurons control a defensive
860 emotion state. *eLife* 4:e06633.
861 74. Pérez-Gómez A*, et al.* (2015) Innate Predator Odor Aversion Driven by Parallel Olfactory
862 Subsystems that Converge in the Ventromedial Hypothalamus. *Current Biology*
863 25(10):1340-1346.
864 75. Koob GF & Volkow ND (2016) Neurobiology of addiction: a neurocircuitry analysis. *The*
865 *lancet. Psychiatry* 3(8):760-773.
866 76. Russo SJ & Nestler EJ (2013) The brain reward circuitry in mood disorders. *Nature*
867 *Reviews Neuroscience* 14(9):609-625.
868 77. Silva BA, Gross CT, & Graff J (2016) The neural circuits of innate fear: detection,
869 integration, action, and memorization. *Learn Mem* 23(10):544-555.
870 78. Coletta L*, et al.* (2020) Network structure of the mouse brain connectome with voxel
871 resolution. 6(51):eabb7187.
872 79. Salvan P*, et al.* (2023) Serotonin regulation of behavior via large-scale neuromodulation
873 of serotonin receptor networks. *Nature Neuroscience* 26(1):53-63.
874 80. Taylor NL*, et al.* (2022) Structural connections between the noradrenergic and cholinergic
875 system shape the dynamics of functional brain networks. *NeuroImage* 260:119455.

876 81. Zerbi V*, et al.* (2019) Rapid Reconfiguration of the Functional Connectome after
877 Chemogenetic Locus Coeruleus Activation. *Neuron* 103(4):702-718.e705.
878 82. David & Adolphs R (2014) A Framework for Studying Emotions across Species. *Cell*
879 157(1):187-200.
880 83. Flavell SW, Gogolla N, Lovett-Barron M, & Zelikowsky M (2022) The emergence and
881 influence of internal states. *Neuron* 110(16):2545-2570.
882 84. Jaric I*, et al.* (2022) The rearing environment persistently modulates mouse phenotypes
883 from the molecular to the behavioural level. *PLoS Biol* 20(10):e3001837.
884 85. Jaric I*, et al.* (2024) Using mice from different breeding sites fails to improve replicability
885 of results from single-laboratory studies. *Lab Anim (NY)* 53(1):18-22.
886 86. Usui T, Macleod MR, McCann SK, Senior AM, & Nakagawa S (2021) Meta-analysis of
887 variation suggests that embracing variability improves both replicability and
888 generalizability in preclinical research. *PLoS Biol* 19(5):e3001009.
889 87. Chang C-H & Gean P-W (2019) The Ventral Hippocampus Controls Stress-Provoked
890 Impulsive Aggression through the Ventromedial Hypothalamus in Post-Weaning Social
891 Isolation Mice. *Cell Reports* 28(5):1195-1205.e1193.
892 88. Manzano Nieves G, Bravo M, & Bath KG (2023) Early life adversity ablates sex
893 differences in active versus passive threat responding in mice. *Stress*:1-32.
894 89. Spring S, Lerch JP, & Henkelman RM (2007) Sexual dimorphism revealed in the
895 structure of the mouse brain using three-dimensional magnetic resonance imaging.
896 *NeuroImage* 35(4):1424-1433.
897 90. Bruce MR*, et al.* (2021) Sexually dimorphic neuroanatomical differences relate to ASD-
898 relevant behavioral outcomes in a maternal autoantibody mouse model. *Molecular*
899 *Psychiatry* 26(12):7530-7537.
900 91. Holz NE*, et al.* (2023) A stable and replicable neural signature of lifespan adversity in the
901 adult brain. *Nature Neuroscience*.
902 92. Lerch JP*, et al.* (2011) Maze training in mice induces MRI-detectable brain shape
903 changes specific to the type of learning. *NeuroImage* 54(3):2086-2095.
904 93. Ashburner J*, et al.* (2012) SPM8 manual.
905 94. Ashburner J*, et al.* (2014) SPM12 manual.
906 95. Carter CS, Lesh TA, & Barch DM (2016) Thresholds, Power, and Sample Sizes in
907 Clinical Neuroimaging. *Biological Psychiatry: Cognitive Neuroscience and Neuroimaging*
908 1(2):99-100.
909 96. Mumford JA (2012) A power calculation guide for fMRI studies. *Social Cognitive and*
910 *Affective Neuroscience* 7(6):738-742.

911 97. Vandekar SN & Stephens J (2021) Improving the replicability of neuroimaging findings by
912 thresholding effect sizes instead of p-values. 42(8):2393-2398.
913 98. Lehallier B*, et al.* (2012) Brain Processing of Biologically Relevant Odors in the Awake
914 Rat, as Revealed by Manganese-Enhanced MRI. *PLoS ONE* 7(10):e48491.
915 99. Petrus E, Saar G, Daoust A, Dodd S, & Koretsky AP (2021) A hierarchy of manganese
916 competition and entry in organotypic hippocampal slice cultures. *NMR in Biomedicine*
917 34(4).
918 100. Bartelle BB, Szulc KU, Suero-Abreu GA, Rodriguez JJ, & Turnbull DH (2013) Divalent
919 metal transporter, DMT1: A novel MRI reporter protein. *Magnetic resonance in medicine*
920 70(3):842-850.
921 101. Duffy KA, McLaughlin KA, & Green PA (2018) Early life adversity and health-risk
922 behaviors: proposed psychological and neural mechanisms. 1428(1):151-169.
923 102. Hakamata Y, Suzuki Y, Kobashikawa H, & Hori H (2022) Neurobiology of early life
924 adversity: A systematic review of meta-analyses towards an integrative account of its
925 neurobiological trajectories to mental disorders. *Frontiers in Neuroendocrinology*
926 65:100994.
927 103. Hammelrath L*, et al.* (2016) Morphological maturation of the mouse brain: An in vivo MRI
928 and histology investigation. *NeuroImage* 125:144-152.
929 104. Brigman JL, Mathur P, Lu L, Williams RW, & Holmes A (2009) Genetic relationship
930 between anxiety-related and fear-related behaviors in BXD recombinant inbred mice.
931 20(2):204-209.
932 105. Noldus LPJJ, Spink AJ, & Tegelenbosch RAJ (2001) EthoVision: A versatile video
933 tracking system for automation of behavioral experiments. *Behavior Research Methods,*
934 *Instruments, & Computers* 33(3):398-414.
935 106. Fox J & Weisberg S (2019) An R Companion to Applied Regression.
936 107. Lenth RV (2022) emmeans: Estimated Marginal Means, aka Least-Squares Means.
937 108. Pinheiro J, Bates D, & Team RC (2022) nlme: Linear and Nonlinear Mixed Effects
938 Models.
939 109. Pinheiro JC & Bates DM (2000) Mixed-Effects Models in S and S-PLUS.
940 110. Posit t (2022) RStudio: Integrated Development Environment for R.
941 111. Team RC (2022) R: A Language and Environment for Statistical Computing.
942 112. Wickham H (2016) ggplot2: Elegant Graphics for Data Analysis.
943 113. Wickham H*, et al.* (2019) Welcome to the Tidyverse. 4(43):1686.
944 114. Tyszka JM, Readhead C, Bearer EL, Pautler RG, & Jacobs RE (2006) Statistical diffusion
945 tensor histology reveals regional dysmyelination effects in the shiverer mouse mutant.
946 *NeuroImage* 29(4):1058-1065.

947